Development of Isotopic Carbon Labeling Diagnostic for Electric Propulsion

IEPC-2022-163

Presented at the 37th International Electric Propulsion Conference
Massachusetts Institute of Technology, Cambridge, MA USA
June 19-23, 2022

Sean Clark[1], Joshua Tompkins[2], Keita Nishii[3], Joshua L. Rovey[4], and Deborah Levin[5]

University of Illinois, Urbana-Champaign, Illinois, 61801, USA

Carbon contamination sputtered from graphite lined vacuum facilities obscures erosion and deposition measurements of carbon-based thruster components during electric propulsion wear tests. The uncertainty in lifetime analysis models associated with facility effects compounds as thrusters move towards higher powers and the associated rates of backsputtered facility contamination increase. A non-intrusive diagnostic decoupling facility and thruster sourced carbon is necessary in obtaining erosion rates of thruster components and accurate lifetime analysis of high-powered systems. Isotopic labeling using $^{13}\mathrm{C}$ may be used to track the transport of carbon throughout the thruster-facility environment. We report the synthesis of high concentration $^{13}\mathrm{C}$ monoliths to facilitate carbon tracking during electric propulsion wear testing. Monoliths were synthesized using powdered $^{13}\mathrm{C}$ and a 5 wt% furan resin binder with expected concentrations of 96% $^{13}\mathrm{C}/\mathrm{C}$.

I. Introduction

High powered electric propulsion (EP) systems are a critical component of an affordable and evolvable architecture for expanding human presence beyond Earth orbit. With progression of in-space energy harvesting, high powered thruster strings such as the 40kW system proposed for the lunar gateway, utilizing NASAs 14kW AEPS Hall Thruster, can be realized. Evaluation of a thruster's performance and lifetime is contingent upon successfully de-coupling ground-based facility effects to accurately represent its on-orbit operation. Facility effects range from pressure-based effects, electrical coupling to conductive facility walls, and backsputtered contamination of facility materials that are not present in the space environment [1]. The most widely investigated facility effects are pressure induced effects. Some of these pressure effects include an increase in CEX ions with increasing background pressures [2], shifting of the acceleration region location causing a bowed potential profile around the exit plane, which provides a path for CEX ions to accelerate back towards the thruster [3]. Both effects can lead to variation in the erosion profiles of thruster components. Electrical coupling impacts plume properties offering an alternative recombination site along facility surfaces [4], leading to the sputtering of facility materials on the sides of vacuum chambers. Additionally, this electrical coupling to facility walls has shown to have effects on the cathode coupling voltage [5], possibly leading to a shift in the acceleration region and the accompanied variation in potential profiles surrounding the thruster exit plane. Facility contamination effects stem from backsputtered carbon from facility liners depositing on thruster surfaces causing two issues for accurate lifetime analysis of EP systems: (1) masking true erosion profiles of carbon-based thruster components and (2) obscuring the amount of carbon deposited films within the thruster related to erosion of the thruster itself. These conductive films can induce

---

[1] Graduate Student, Department of Aerospace Engineering, saclark5@illinois.edu.
[2] Graduate Student, Department of Aerospace Engineering, jrt8@illinois.edu
[3] Postdoctoral Researcher, Department of Aerospace Engineering, knishii@illinois.edu
[4] Associate Professor, Department of Aerospace Engineering, rovey@illinois.edu
[5] Associate Professor, Department of Aerospace Engineering, deblevin@illinois.edu

thermal stresses on dielectrics and cause electrical shorting of normally isolated components [6]. As EP systems move towards higher powered capabilities, the impact of all facility effects will increase, as does the need to effectively de-couple these artifacts to understand the on-orbit performance and lifetimes of these systems.

As part of a larger campaign to eliminate or correct for facility artifacts from EP systems, one of the objectives is to validate numerical simulations that will enable extrapolation of facility-tested thruster performance to in-space performance. Thrusters are designed for lifetimes on the order of several tens of thousands of hours. Flight verification of such systems relies on numerical modeling to obtain performance and lifetimes as testing for these extended periods is not feasible. Therefore, our team is simultaneously developing a transport model leveraging both Particle-In-Cell (PIC) and Direct Simulation Monte Carlo (DSMC) techniques. PIC is a well-established kinetic approach used to compute the time-evolving characteristics of charged particles in a plasma and their interactions with the induced electric field, while the particle based DSMC approach is required to effectively model collisionality. The Cuda-based Hybrid Approach for Octree Simulations (CHAOS) code, developed by Lambunathan and Levin [7], utilizes both approaches and has been extensively used for modeling the in-space environment [8–10]. The expansion of this code to include facility-based effects will use the results of the experimental campaign to verify and validate their transport models and lifetime analysis.

Backsputtered carbon contamination masking erosion and deposition measurements is of particular interest to this study. Current methods to subtract facility contamination effects from erosion profiles leverage quartz crystal microbalances to obtain average backsputter rates. These microbalances are used in tandem with numerical models to obtain estimations of erosion in life limiting thruster components [11]. However, these microbalances fail to encapsulate carbon transport through the near-field plume and are unable to provide direct measurements of redeposition of thruster-based carbon back onto thruster surfaces. Additionally, carbon-based thruster components have been replaced with dissimilar materials, such as Molybdenum [6,12]. However, this introduces uncertainty and disparate erosion rates. Thus, a new, non-invasive, and carbon-based diagnostic to track transport is needed. The focus of this study is on the development of such a diagnostic that can map the transport of facility and thruster-based carbon through isotopic labeling. Monoliths containing high concentrations of $^{13}\mathrm{C}$ will be synthesized and used as sputtering targets in the thruster-facility environment. The deposition of the tracer, $^{13}\mathrm{C}$, onto witness plates placed on thruster surfaces and throughout the facility can be analyzed through mass spectrometry to capture both transport through the plume and track deposition from specific thruster components.

Two configurations of the diagnostic are shown in Fig. 1. The labeled carbon targets can be placed within the plume and utilize a directed sputtering technique as shown in Fig. 1a. Facility-based and labeled carbon are deposited onto witness plates, creating a map of carbon deposition. Additionally, the labeled targets and witness plates can be placed on thruster surfaces as shown in Fig. 1b. This enables direct tracking of sputtered material from specific thruster components to its deposition within the thruster itself. Mapping of the $^{13}\mathrm{C}/\mathrm{C}$ deposition within the thruster allows quantification of the conductive film deposition sourced from thruster components. Such

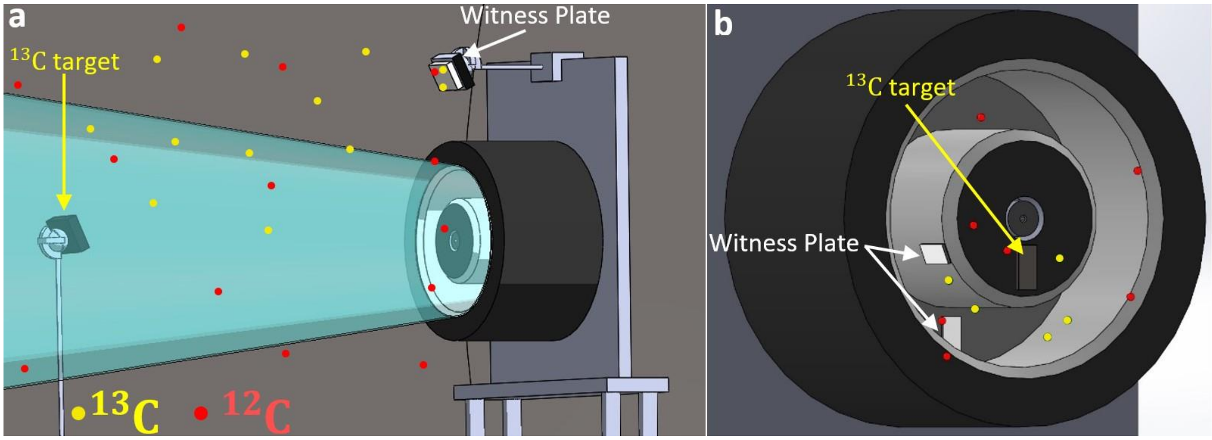

Figure 1. (a) Configuration 1 of carbon tracking diagnostic. Targets are placed within the plume of the thruster and witness plates placed throughout the facility or on thruster surfaces. (b) Configuration 2, the isotopic targets are placed on thruster surfaces to track erosion and deposition from specific thruster components

a diagnostic can be used during experiments investigating pressure-based and electrical facility effects to identify how these relations impact the erosion properties of life limiting thruster components.

II. Analytical Investigation of Proposed Approach

Analytical modelling was undertaken to determine the effects of target placement with respect to the ion source and witness plate, incident angle of bombarding ions, how the type of carbon material would affect the sputtering profile, and how these parameters contribute to the bombardment time and requisite target thickness.

A. Ion Source Characteristics

The initial demonstration test of the diagnostic will be conducted using a Busek BHT200 (operating power of 200W, discharge voltage of 250V), utilizing a directed sputtering approach as shown in Fig. 1a. Operational parameters of the BHT200 at an operating pressure of 4x10^{-6} Torr provided by Nakels et al. 2007 [13] were used to estimate the Xenon ion current arriving at the target plate. Fig 2. depicts the ion current density normalized by the peak value of approximately 100 A/m^2. The ion current density reduces with the typical inverse power profile across the 45cm span. As such, to provide the highest level of ion flux to the target plate it will need to be relatively close to the exit plane of the ion source. For the purposes of the analytical model, the ion current distributions in Fig 2 were utilized to determine the sputtered mass arrival rate and time-to-deposition of the sputterant at a witness plate for singly charged Xenon bombardment. The singly charged assumption was based on data provided by Hillier et al. 2011 [14] where singly charged species represented 97.5% of the total Xenon observed.

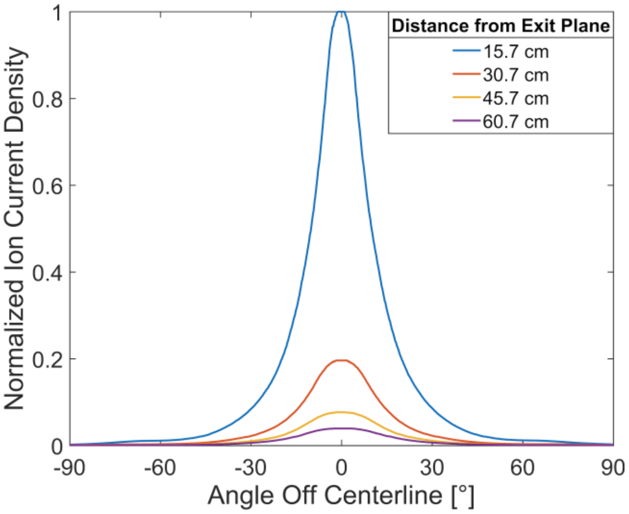

Figure 2. Normalized Ion Current Density of Busek BHT200 Ion Source for Xenon.

B. Deposited Carbon Thickness Evaluation

The dimensional requirements of labeled monoliths are determined by the mass and thickness requirements of concentration analytics. Time of flight secondary ion mass spectrometry (ToF-SIMS) and isotope ratio mass spectrometry (IRMS) will be used to determine concentrations of the bulk monoliths and thin film deposits. ToF-SIMS can determine concentrations from film thickness on the order of several nanometers, while IRMS requires sample masses of tens of µg. Additionally, development of a general diagnostic includes considerations for long duration wear tests and the full mapping of thruster surfaces in low C flux regions, such as the anode [15]. Therefore, scalability of the monolith dimensions should also guide the manufacturing approach. The deposition layer thickness, Δx, can be defined through a 60 µg sample mass for IRMS through Eqn. 1.

$$\Delta\mathrm{x} = \frac{m_{IRMS}}{\mathrm{A}_w \rho_{aC}} \tag{1}$$

Where A_w is the surface area of the collection plate and ρ_{aC} is the density of amorphous carbon. The theoretical density of amorphous carbon is a function of sp^3 concentration and defined by Chinkanjanarot 2014 [16] as the following:

$$\rho_{aC} = 1.92 + 1.37 f_{sp^3} \tag{2}$$

For a conservative estimate, an upper limit on the required deposition thickness is obtained by setting the fraction of sp^3 bonds, $\mathrm{f}_{\mathrm{sp}^3}$, to zero. For a 60 µg sample and 4 cm^2 collection area, the corresponding thickness is 80 nm.

C. Graphitic Material Sputtering Characteristics

With an understanding of the requisite deposition thickness at the witness plate needed for characterization it is important to now understand the sputtering profile of carbon materials to minimize the bombardment time. A study by Williams et al. in 2003 [17] investigated the sputtering profiles of pyrolytic graphite (PG) and carbon-carbon composites (C-C) for ion energies between 200 and 1000 eV and incidence angles from 0° (normal incidence) to 60° with their results mapping the differential sputtering yield of these materials. Fig 3 presents the directional sputtering yield of PG & C-C with respect to the polar ejection angle, α, for the ion energies, E_i, investigated at the incidence angle, θ_i, presenting the greatest sputtering.

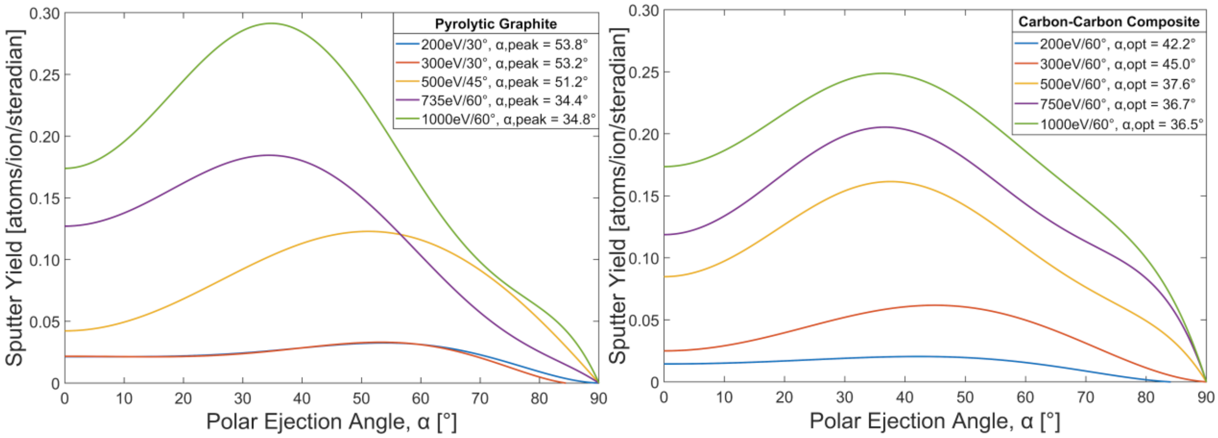

Figure 3. Sputter yield variation with E_i, and θ_i and corresponding optimum polar ejection angle: (a) Pyrolytic Graphite (b) Carbon-Carbon Composite.

Across the range of E_i, the maximum PG sputter yield varies with θ_i whereas the C-C always has maximum sputter yield at 60°. However, for the energy range pertinent to proposed experimental tests, 200 eV to 300 eV, PG showed maximum sputtering at $\theta_i = 30°$ with the most sputtered material ejected at angles of 53.8° and 53.2°, respectively. Similarly, C-C at the same energies has maximum sputtering at $\theta_i = 60°$ and the most sputtered material ejected at an α of 45.0° for 200 eV and 37.6° for 300 eV. Consideration of the differential sputtering yield provides the means by which to ideally orient the target sample in the ion plume to preferentially achieve maximal sputtering delivery to the witness plate should be obtained for an α between 42.2° and 53.8°, which are the bounds of 200 eV and 300 eV sputtering of PG and C-C. Characterization of the synthesized samples is expected to provide a more thorough understanding of the type of graphitic material obtained which should further narrow the optimal orientation needed for ion bombardment testing.

D. Time-to-Deposition and Target Thickness

Knowing the properties of Xenon sputtered carbon materials and with the established ion source and graphitic material characterization it is now possible to evaluate the time-to-deposition required for carbon atoms sputtered from the target to deposit at the witness plate. The analytical model for calculating the mass arrival rate, R, was similar to the approach by Williams et al. [17] and is defined as the following:

$$\mathrm{R}(\alpha) = \mathrm{y}(\alpha)\Omega_{tw}\frac{\mathrm{I}_b}{q}\frac{\mathrm{M}_C}{\mathrm{N}_A} \tag{3}$$

where y(α) is the differential sputter yield in atoms/ion/sr which is a function of the polar ejection angle, Ω_{tw} is the solid angle between the target and witness plates, I_b is the ion beam current , q is the charge of the ions, M_c is the atomic mass of carbon, and N_a is Avogadro's number. The sputtered mass arrival rate at the witness plate is dependent upon the physical parameters of the system discussed previously such as the variance in ion current density with target spacing from the ion source. Assuming the mass arrival rate is reasonably representative of the material striking the witness plate, then the time-to-deposition, t, can be determined by Eqn. 4.

$$t = \frac{\Delta x A_w \rho_{ac} S}{R(\alpha)} \tag{4}$$

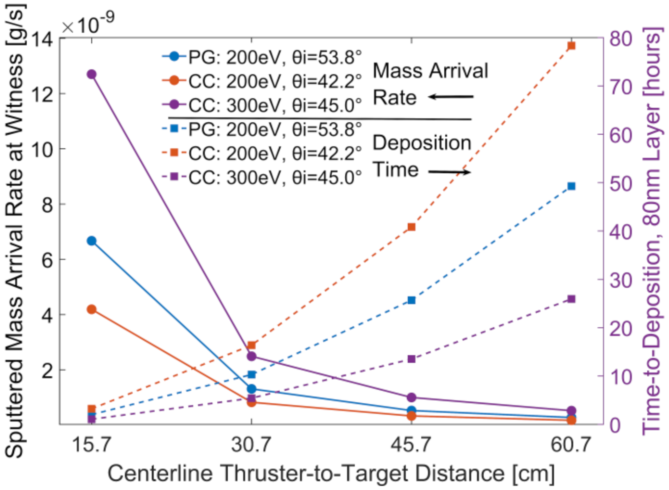

Figure 4. Sputtered mass arrival rate and corresponding Time-to-Deposition for Xe⁺ bombardment of Pyrolytic Graphite and Carbon-Carbon composite.

Where S is the mean sticking coefficient of the substrate. Fig. 4 depicts the sputtered mass arrival rate at the witness plate and the corresponding time-to-deposition for an 80 nm thick film for a target along the centerline of the ion source. Assumptions included: a sticking coefficient of 0.8, deposition collection area of 4 cm^2, an aC density of 1.92 g/cm^3 , and a target-witness spacing of 10 cm. Since the differential sputtering profiles of PG at 200 and 300eV were so similar, only the plot 200 eV values were utilized in determining the time-to-deposition. The stark drop-off in ion current density, as depicted in Fig. 2, presents a large disparity in the time-to-deposition at the witness plate. At a target distance of 15.7 cm, 200 eV Xenon bombardment of PG and C-C require 2.03 and 3.22 hours of exposure, respectively, while 300 eV C-C only requires 1.067 hours. However, at a target distance of 60.7 cm, these times increase up to 49.3 hours for 200 eV PG, and 78.3 and 25.9 hours for 200 eV and 300 eV C-C: a 23.3-fold increase in time-to-deposition. Having an idea of the time required to obtain the 80 nm layer is crucial to validate a minimum required thickness for the target. An estimate of this required minimum thickness for the target monoliths, T_M, is given by the following:

$$T_M = \frac{Y M_C I_b}{A_t \rho_M q} t \tag{5}$$

where Y is the total sputtering yield in atoms/ion, A_t is the cross-sectional area of the target sample, ρ_M is the density of the monolith material, and t is the time-to-deposition given by Eqn. 4. The thicknesses required for isotopic sputtering targets were estimated based on the results presented in Fig 4 and the reported total sputtering yield of the materials for their corresponding incident energies [17]. Based on the measured isotopic target material density of 1.41 g/cm^3, the minimum target thicknesses required to deposit a single 80 nm layer witness film are 7.47 µm for PG at 200 eV and 6.96 µm, and 5.48 µm for C-C at 200 and 300 eV at a target-source spacing of 15.7 cm. Of course, this idealized approach will underestimate the minimum time required for deposition and will necessitate modification as parameters become clearer. Consequently, these estimated minimum target thicknesses per deposition run are lower than what should be required.

E. Key Takeaways from Analytical Model

The key insight offered by the analytical modelling approach is establishment of baselines for target synthesis and how to approach experimental design to minimize ion bombardment time to achieve the desired carbon deposition thickness. This shows that sputtering of isotopically labeled carbon targets placed in the ion plume of a Hall thruster is feasible and the time-to-deposition short provided

- Directional sputtering of ^{13}C targets is bounded by the range established for PG and C-C at 200-300 eV.
- The sticking coefficient is sufficiently high and deposited carbon is shielded from the plume.
- The experimental setup can be reasonably matched to the analytical model's parameters.

Aspects which could offer significant deviations from this analysis relate to disparities in the crystalline structure of the synthesized isotopic carbon, which will require thorough characterization, and target-witness plate placement. As noted, the data reported in Fig 4 is for a target-witness spacing of 10 cm. If currently unidentified issues with the experimental setup prohibit this placement, then the time-to-deposition will be augmented based on the difference in the solid angle between the two plates. If plate spacing where to increase, the greatest impact this will have on the experimental side is the requirement for longer ion bombardment which will increases cost, specifically with respect to Xenon usage, and cause additional erosion of the target. However, providing sample synthesis creates isotopic targets of significant thickness then additional erosion of the target can be largely ignored as the "per-run" degradation is on the order of microns. Extrapolating these analytical results to predict the time-to-deposition for isotopically labelled pole covers is not currently feasible given the stark variance in ion energies during sputtering. Still, it is apparent the pole covers will take considerably longer to erode an appreciable mass and will require extended operation to establish degradation for reliability modelling, resulting in higher propellant costs. Longer duration tests may also see additional witness deposition of ^{12}C eroded from the vacuum facility walls; however, the characterization methods proposed can accurately distinguish concentrations for even miniscule amounts of isotopes once properly calibration, and therefore is not of concern at this time.

III. Technique Development

A. Carbon Materials Common to Thruster-Facility Environment

Irradiation of materials by ion bombardment causes the microstructure of the surface to undergo amorphization. Depending on the initial microstructure of the material, the time until a steady state sputtering profile will vary. Uncertainties in the sputtering profiles and time until a steady state is reached can be dependent on the crystal orientation, material density, porosity, grain size and the surface topology of the material [18]. Carbonic materials found in the thruster-facility environment can include highly oriented pyrolytic graphite (HOPG) or C-C composites used in optics of ion thrusters, high density ($\rho > 1.8\ g/cm^3$) isotropic graphite used for cathode keepers and pole covers, and traditional ABAB stacked synthetic graphite or Graphoil used for beam dumps. The microstructure between these carbon materials varies from perfectly stacked graphene layers found in HOPG to turbostratic or amorphous structures for C-C composites dependent on the filler material used. The density and porosities of these materials varies significantly between each type of carbon material and can vary for each type based on the manufacturing method. To effectively decouple carbon-based facility contamination from thruster erosion and deposition to reduce uncertainty in lifetime analyses full material characterization and evolution of the characteristics should be accounted for when identifying differential and sputter yield measurements. HOPG, holds the highest density of the materials approaching 2.25 $\mathrm{g/cm^3}$ and correspondingly near zero porosity. HOPG is highly anisotropic, having high electrical and thermal conductivity properties in plane, while having low conductivity properties out of plane. Isotropic graphite used for thruster components has fine grain size and high densities with typical porosities ranging from 15-35%. The structure of isotropic graphite is defined through a micro particle structure of randomly oriented local domains of stacked graphene layers, lending itself to equivalent strengths and transport properties along both axes. C-C composites are more porous materials with densities typically ranging from 1.4-1.9 $\mathrm{g/cm^3}$. Ideally, the manufacturing method of high concentration $^{13}\mathrm{C}$ monoliths to be used as a tracer material would be catered towards matching the properties and time till steady state sputtering of the specific type of carbon material under analysis (as shown by Fig. 1b). This would ensure near equivalent total and differential sputter yields as well as similar local electromagnetic fields, assisting in uncovering the mechanisms responsible for erosion of these components.

B. Synthesis Routes for Isotopically Labeled Monoliths

For high concentration isotopically labeled materials we have identified three possible methods: labeled polymer films, chemical vapor deposition, and powdered metallurgy. C-C composites are primarily synthesized from carbon fibers surrounded by a carbonic matrix. The carbon fibers themselves are created by stretching and thermally treating poly(acrylonitrile) to temperatures below the onset of graphitization (2200℃), where the carbon matrix can include soft carbons (graphite) or hard, amorphous carbons (coke). Labeled polymers such as poly(ethylene) can also be used to obtain graphitic materials by including catalysts such as boron oxide [19]. Fully labeled, $^{13}\mathrm{C}$ acrylonitrile and poly(ethylene) are commercially available and can be obtained through Cambridge Isotopes and Polymer Source Inc. HOPG is synthesized through chemical vapor deposition of heavy methane and has been shown to be capable of producing near unity concentrations of isotopically labeled monoliths (~99.5% $^{13}C/C$) for sub-micron films [20,21]. The first use of the proposed diagnostic will be to decouple carbon contamination from the facility as shown in Fig. 1a. Graphite facility liners are seldom replaced and will have a fully amorphized surface layer and, in this context, the first phase of the diagnostic will use an amorphous bulk material to match properties of the heavily irradiated facility structure. As the technology develops, matching conductivity properties of tracer materials through higher cost methods such as CVD HOPG and synthesis of high $^{13}\mathrm{C}$ concentration C-C composites may be considered. Thus, the isotopic amorphous carbon tracer will be synthesized through use of a powdered precursor and organic, high carbon content, binding agent. The available ^{13}C precursor is a pyrolyzed algae (CAS#: 14762-74-4) and is known to be a non-graphitizing, hard, carbon powder [22,23]. At hundreds of dollars per gram, thick (mm scale) monoliths can be synthesized for a reasonable cost. This method offers the ability to easily scale the geometry and size of monoliths and has capabilities of synthesizing entire thruster components if conductive properties are similar and distortion of local fields can be minimized.

C. Identified Procedure for Labeled Carbon Monoliths

Hard carbons are often used in capacitors and filtration systems and the synthesis focuses on increasing the surface area of particles and porosity of the bulk material. However, as higher void content leads to higher uncertainty in sputter yields, our goal in synthesis is to obtain high density and low porosity amorphous carbon monoliths. Additionally, as the source of ^{12}C in these monoliths is tied to the amount of organic binder used, the synthesis should include a strong binder capable of producing strong monoliths with minimal binder concentration to maximize the tracer content. Glassy carbon is known for its strength, therefore binding agents such as furan and phenolic resin that vitrify under heat treatment were considered as ideal candidates. Additional binders considered are those common to activated carbon monoliths, which include poly(vinyl alcohol)(PVA) and a mixture of bentonite and methylcellulose. The densification methods considered for these composites included hot compression molding for the thermosetting resins (furan and phenolic resins) and cold compression techniques using a pellet press for initial forming and cold isostatic pressing for further densification. Figure 5 shows a schematic of possible pathways for synthesis of amorphous carbon monoliths.

A significant consideration in the production of monoliths is the mass loss for each step due to the cost of isotopic precursors. It was found during hot compression molding of phenolic-carbon composites that despite lubrication of the mold, the lubricant burned off, the bulk material adhered to the sides of the die and fractured upon removal. While these defects could be removed during future grinding and polishing procedures, the mass loss associated with hot compression molding (~19%) was deemed too significant for hot compression techniques to be pursued. Further, densification through CIP can be conducted under pressures exceeding 200 MPa vastly exceeding the hot compression

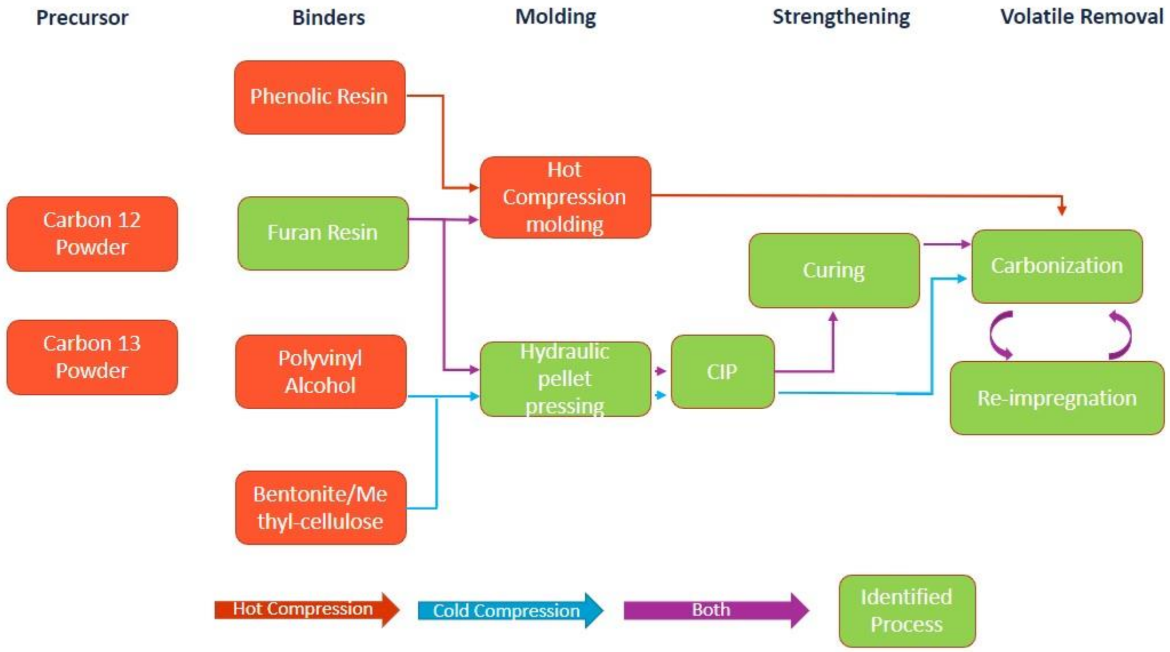

Figure 5. Schematic showing the examined synthesis routines of labeled amorphous carbon monoliths. Red arrows denote pathways specific to hot compression molding only, blue for cold compression techniques and purple for processes that are applicable to all binders or compression techniques. Green boxes denote the identified procedure pathway used for synthesis of labeled monoliths.

techniques and offered higher density a-C monoliths. For the bentonite-methylcellulose binder, stable structures required higher binder fractions than PVA or PFA binders. Below 15 wt% binder concentration, stable structures could not be obtained, thus producing a monolith with isotopic content lower than PVA or PFA composites. PVA composites were found capable of producing monoliths with only 5 wt% binder concentration, but due to full decomposition of the binder and absence of vitrification during thermal treatment, the remaining structure easily fractured, and monoliths could not be used for characterization or future experiments. Therefore, the converged upon procedure synthesizes carbon monoliths using poly(furfuryl) alcohol as a binding agent.

The PFA was obtained from Polysciences. Maleic anhydride (MA) and $^{13}\mathrm{C}$ powder (99% purity) was obtained from Millipore Sigma. To determine a procedure before transferring to the $^{13}\mathrm{C}$ powder, a similar hard $^{12}\mathrm{C}$ was obtained from MSE Supplies LLC. A 50 wt% PFA solution is created with 47.8 wt% acetone as a diluent and 2.2% MA as a catalyst to promote cross-linking during curing. The solution was mixed in a closed container at room temperature for 30 minutes. Composites of 20, 15, 10, and 5 wt% PFA and $^{12}\mathrm{C}$ powder were mixed in a THINKY ARE250 centrifugal mixer at 1400 RPM for two minutes, followed by one minute of de-airing at 1600 RPM. A hydraulic pellet press was used with a 1cm, lubricated, die for initial forming at 30 MPa and held for two minutes. Further densification was performed through variable (75–215 MPa) pressures in the CIP to determine a pressure that offered the highest density green bodies without fracturing the monoliths. Post-densification, PFA targets of similar density were cured at temperatures of 140, 150, 160, 175, and 200℃ for one hour under a 10℃/min heat ramp, followed by compressive tests to identify an optimum curing temperature. To address outgassing from the organic binder during application of the diagnostic, the monoliths were carbonized under an inert atmosphere to remove all volatiles. Carbonization was conducted with a heat ramp of 2℃/min. For every 60℃ ramp cycle through 560℃, the ramp cycle was followed by a 30 min dwell period. This incremental ramp-dwell cycle was used to minimize the porosity development and damage to the internal structure that would result from a high rate of outgassing. After the dwell period following the 560℃ ramp cycle, the temperature was increased to 1000℃, held for 60 min, and allowed to naturally cool to 60℃ over 11 hours.

D. Monolith Synthesis Exploration with $^{12}\mathrm{C}$

Density (or porosity) is a key parameter relevant to both obtaining high concentration $^{13}\mathrm{C}/\mathrm{C}$ for experimental studies and to reduce uncertainty in molecular dynamic sputtering simulations that will be used in the development of PIC-DSMC. Increasing the packing density would result in higher strength monoliths that would minimize the required binder concentration and minimize the porosity. As the binder is the primary source of $^{12}\mathrm{C}$ in the structures, minimization the binder increases the isotopic concentration, which was the primary focus of the experiments. Initial trials for variable binder concentration were purely qualitative. Monoliths were initially formed with a 20 wt% binder. If the structure was stable, a reduction in 5 wt % binder was mixed and pressed. The bulk density of monoliths was determined through an analytical balance and calipers. Seen in Fig. 6, the densities of monoliths prepared from a 10 wt% binder increased with increasing pressure from ~0.99 $\mathrm{g/cm^3}$ at 75 MPa before beginning to plateau at ~1.12 $\mathrm{g/cm^3}$ as pressures approached 215 MPa. Pressures of 240 MPa were also tested but resulted in a high frequency of fracturing during the CIP process.

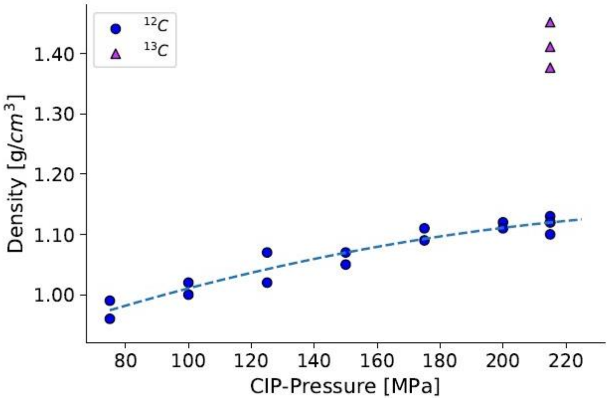

Figure 6. Density variation with increasing pressure. Blue circles denote $^{12}\mathrm{C}$ trials. Purple triangles show the corresponding $^{13}\mathrm{C}$ densities after milling to a particle size distribution between 100-300 nm.

The correlation between curing temperature and compressive strength of the 10 wt% binder composites was investigated. To obtain compressive strengths, the monoliths were placed on a hydraulic press and compressed at 1mm/min until fracture. The results of curing at 140-200℃ are given in Table 1. Furan rings begin to decompose at temperatures exceeding ~170℃ and below these temperatures, mass loss is associated with evaporation of $\mathrm{H_2O}$ [24]. Thus, little variation in strength with curing temperature was expected for temperatures between 140-175℃. The mass loss of each sample varied from 1.2% to 1.7% with increasing temperatures, but no trend in strength and temperature was able to be discerned for temperatures below the decomposition temperature of the furan rings. All targets held compressive strengths between 60 to 70 MPa, below the decomposition temperature. Agglomeration of particles before being charged into the pellet die could have led to variations in porosity and the internal structure, masking any slight variations in strength at different temperatures. At 200℃ the compressive strength dropped to 53.2 MPa. The high strengths associated with the 10 wt% binder prompted a further reduction in the binder concentration. Monoliths constructed using 5 wt% binder, under 215 MPa, and cured at 150℃ and 250℃ yielded compressive strengths of 12.50 MPa and 4.71 MPa, respectively. As the monoliths were still stable a 5 wt% binder concentration was used in ^{13}C trials to maximize the isotopic concentration.

Table 1 Compressive strength of ^{12}C monoliths cured at variable temperatures

Binder Concentration (% wt)	ρ (g/cm^3)	Temperature (℃)	σ (MPa)
10	1.11	140	65.76
10	1.12	150	63.21
10	1.09	160	67.91
10	1.10	175	61.36
10	1.08	200	53.15
5	1.10	150	12.50
5	1.07	250	4.71

The full range of the diagnostic includes capabilities of tracking sputtered isotopic material from thruster surfaces. Therefore, the monoliths must be able to withstand surface temperatures of thruster components. The front pole covers of NASA's 12 kW AEPS thruster reaches temperatures of ~270℃ and the cathode exceeding 600℃ [25]. Monoliths placed on these surfaces without high thermal treatment will produce significant outgassing. If the rate of volatile release is too high, the internal structure will degrade, and the monoliths will break apart. To prevent both outgassing of the material and to increase the thermal properties, the samples must be carbonized. Six green bodies were thermally treated to 120℃, allowing the resin to set. Bulk densities were obtained and three of the samples were carbonized. The compressive strengths of the carbonized samples were compared to those of the remaining cured monoliths. Carbonization reduced the densities of the monoliths by 2.54 ± 0.59 %, but yielded an increase in compressive strength relative to the cured samples, despite having developed higher porosity (lower density). The average compressive strength of carbonized samples was 7.83 ± 1.6 MPa, while the low temperature cured samples held an average compressive strength of 5.02 ± 0.59 MPa. These results suggest vitrification of the furan resin that would create a strong matrix to bind the isotopically labeled carbon when transferring the process to the ^{13}C precursor. Additionally, curing at a lower temperature of 120℃ yielded lower compressive strengths relative to the monolith cured at 150℃ (Table 1) using the same 5 wt% binder concentration. Therefore, the curing process for ^{13}C structures will be conducted at 150℃ to increase the polymerization of the binder before carbonization.

Table 2 Strengths of cured and carbonized ^{12}C monoliths

Carbonized	ρ (g/cm^3)	σ (MPa)
Y	1.06	7.14
Y	1.06	6.30
Y	1.03	10.05
N	1.11	5.74
N	1.09	4.30
N	1.09	5.00

E. Monolith Synthesis Exploration with ^{13}C

Initial monoliths synthesized from the ^{13}C precursors were brittle and easily fractured upon handling, with densities comparable to those of the ^{12}C (~1.11 g/cm^3). The discrepancy in strength was determined to be the variation in average particle size (APS) between the ^{13}C and ^{12}C precursors. Multiple scanning electron microscope (SEM) images were taken of each sample and the APS was determined through processing with ImageJ. The ^{12}C showed a near uniform distribution, with $APS_{12} = 4.59 \pm 1.61$μm. The ^{13}C precursor was right skewed, with $\mathrm{APS}_{13} = 30.27 \pm$

36.42μm, and a significant fraction of particles exceeding 100μm. A larger particle size reduces the available surface area for the binder to coat and bond, reducing the strength of the monoliths. To reduce the particle size, the $^{13}\mathrm{C}$ precursor was milled in an ethanol solution with a horizontal ball mill for 20 hrs, using 10mm zirconia media. Post milling, the solution was dried in an incubator overnight at 68℃. SEM images of the unprocessed $^{12}\mathrm{C}$ and $^{13}\mathrm{C}$ are shown in the top row of Fig 6. The bottom row shows the milled $^{13}\mathrm{C}$ precursor. Capillary forces during the drying process cause individual particles to agglomerate into large flat platelets as seen in Fig. 7c. A high magnification image of a platelet showed that the particles were reduced to a particle size distributed between ~100-300nm. For full wetting of individual particles with the PFA, the large agglomerates should be dispersed before mixing with the binder. Deagglomeration of carbon black through sonication in an ethanol solution has been shown to break agglomerates to ~300nm [26]. The milled material was sonicated for 1 hr before mixing with the PFA.

Pressing of the nanopowder resulted in stable $^{13}\mathrm{C}$ monoliths with a relatively lustrous finish as shown in Fig. 8 and significantly higher density as shown in Fig. 6. The average density of the green bodies was found to be $1.41 \pm 0.31\ \mathrm{g/cm^3}$, a 29% increase relative to the initial labeled monoliths. Reducing the $^{13}\mathrm{C}$ particle size is a necessary step for obtaining sufficiently strong, low porosity structures. Furan binder ($\mathrm{C_5H_6O_2}$) contains a $^{12}\mathrm{C}$ mass fraction of 61.2%. Using a 5 wt% binder and assuming equal amounts of $^{12}\mathrm{C}$ and $^{13}\mathrm{C}$ are removed as CO, $\mathrm{CO_2}$, and $\mathrm{CH_4}$ during carbonization, the expected isotopic concentration ($^{13}\mathrm{C/C}$) is 95.9%. Figure 8 shows monoliths synthesized with variable concentration of $^{13}\mathrm{C}$ precursor. Minor edge defects can be seen in Fig. 8b, and 8c that are a result of the $^{13}\mathrm{C}$ nanopowder flowing through the interface between the die and plunger during initial formation. Mass lost through the interface results in low density regions at the edge, which fractures due to the surface roughness of the die walls as the samples are ejected from the die. These defects can be eliminated by simple polishing processes or obtaining a die set with less clearance between the plunger and die.

The specific synthesis procedure to create strong, high concentration $^{13}\mathrm{C}$ labeled monoliths as shown by Fig. 8 is summarized below:

1. Mill $^{13}\mathrm{C}$ precursor for 30 hrs until a nanopowder with particle sizes distributed between 100-300 nm is obtained.
2. Sonicate milled powder in acetone for 1 hr to de-agglomerate and disperse particles.
3. Add 5 wt% PFA from the 47.8 wt% PFA binder solution to the sonicated $^{13}\mathrm{C}$ slurry.
4. Mix the slurry at 1400 RPM for two minutes followed by 1 min of de-airing at 1600 RPM
5. Dry the mixed binder-powder solution at 68℃
6. Load the dried powder-binder mixture into a die and press at 30 MPa for 3 min.
7. Press the green body at 215 MPa for 5 min in a CIP
8. Cure the green bodies in a muffle furnace for 1 hr at 150℃ under a 0.5℃/min heat ramp, let naturally cool to room temperature
9. Carbonize cured monoliths at 1000℃ with a 2℃/min ramp rate. Include 30-minute dwell cycles between each 60℃ increment up to 560℃ to allow time for volatiles to slowly outgas.

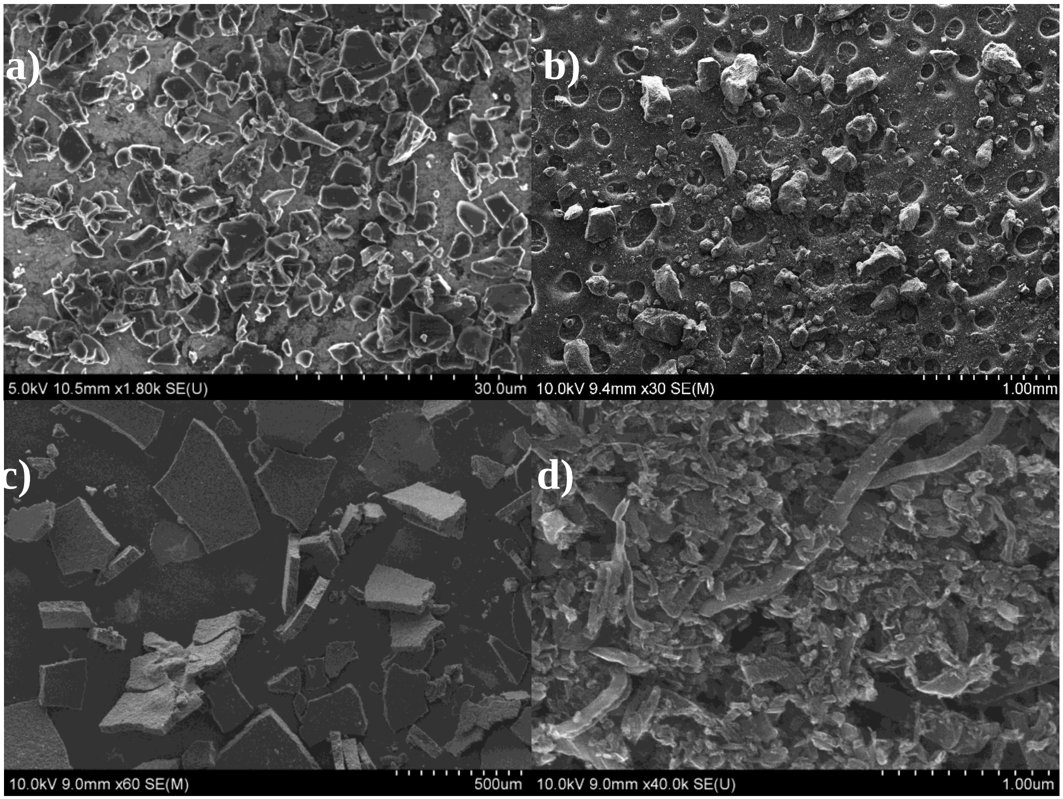

Figure 7. The top row shows images of the unprocessed ^{12}C (a), ^{13}C (b), where a large discrepancy in particle size can be seen between the two images noting (a) has a scale of 30 µm and (b) of 1 mm. The bottom row shows the processed ^{13}C. Flat platelets (c) are formed from the nanoscale powder (d) agglomerating during the drying process.

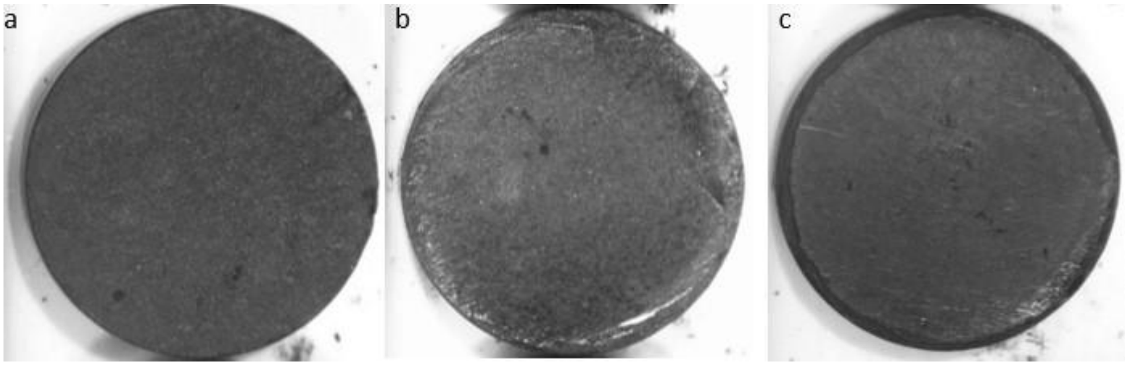

Figure 8. Carbon monoliths created with (a) 100% ^{12}C, (b) 50% ^{13}C, (c) 100% ^{13}C. Monoliths are 1cm in diameter and 0.2cm in thickness. Slight edge defects can be viewed in materials synthesized with ^{13}C.

IV. Conclusion

To decouple backsputtered facility contamination effects from the erosion profiles and conductive film deposition of thruster components, the development of a new isotopic carbon tracing diagnostic is being pursued. The diagnostic will be used to map the transport of carbon throughout the thruster-facility environment by collecting deposition sourced from the facility, thruster, and from labeled monoliths. The first phase of the diagnostic development, obtaining a procedure to synthesize high concentration isotopically labeled carbon monoliths, has been identified. Variable pressures and thermal treatment conditions were investigated to produce stable, high-density monoliths, with minimal binder concentration. Densification under 30 MPa for initial forming and CIP pressures of 215 MPa was found to produce the highest density monoliths without fracture. Curing temperatures of 150℃ increased the polymerization and the resultant strength of the samples. Carbonizing at 1000℃ under a 2℃/min ramp was used to eliminate volatiles, minimizing outgassing during a future application of the diagnostic as well as to increase thermal properties, ensuring the labeled material could be placed on hot (>500℃) thruster surfaces. Milling of the $^{13}\mathrm{C}$ precursor was found to be a critical step in obtaining stable isotopically labeled monoliths. Reducing the APS from ~30μm to a nanopowder with a distribution between 100-300nm increased the density of the labeled monoliths by 29%, obtaining an average density of 1.41 $\mathrm{g/cm^3}$. A minimum binder concentration of 5 wt% was found, resulting in expected isotopic concentrations of ~96%. The identified method can be easily scaled to meet deposition needs dependent on the collection location and testing environment.

V. Future Work

Before a demonstration of the diagnostic can be performed, the concentration analytic must first be calibrated for thin film depositions that will be collected during EP testing. The primary concentration analytic, ToF-SIMS, is known to experience mass fractionation that preferentially inflates peaks of lighter isotopes due to the matrix surrounding the analyte ($^{13}\mathrm{C}$). IRMS, which combusts the carbon material under an oxygen atmosphere, determines isotopic ratios from the resulting $\mathrm{CO_2}$ gas. As IRMS has no matrix dependency that must be matched to a standard reference sample, it will be used to obtain concentrations of the synthesized monoliths and calibrate the ToF-SIMS system. Monoliths that have a known concentration will then be sputter coated onto substrates to be analyzed with IRMS and ToF-SIMS. Variable concentration ($^{13}\mathrm{C/C}$) monoliths have been synthesized from a mixture of both $^{13}\mathrm{C}$ and $^{12}\mathrm{C}$ precursors and are currently undergoing concentration analysis before future sputter coating. As this work is closely intertwined with the development of transport models, experiments will also be conducted to aide in the construction of high-fidelity molecular dynamics carbon sputtering models that will be used to introduce backsputtered carbons into the PIC-DSMC transport models. Existing literature for sputtering of carbon-based materials under xenon bombardment have not considered full material characterization or evolution of sputter relevant characteristics during bombardment. Thus, material characterization of common carbon thruster materials and the isotopically labeled monoliths will be conducted and their evolution tracked during upcoming sputtering trials. These parameters include surface roughness, porosity, hybridized bond ratios, and crystal orientation as well as environmental parameters such as surface temperature and its influence on differential sputter yields. Alongside the experimental work, the transport models are working to extend the CHAOS code to effectively simulate the facility environment. Initial demonstration tests will be conducted at the University of Illinois at Urbana-Champaign, University of Michigan, and Georgia Tech and models are being configured to match the geometry, pumping rates, and background pressures at these test facilities.

Acknowledgments

This work was partially supported by NASA through the Joint Advanced Propulsion Institute, a NASA Space Technology Research Institute, grant number 80NSSC21K1118.

References

[1] Huang, W., Kamhawi, H., Haag, T. W., Ortega, A. L., Mikellides, I. G., Kamhawi, H., Haag, T. W., Ortega, A. L., and Mikellides, I. G. Facility Effect Characterization Test of NASA's HERMeS Hall Thruster.

[2] Walker, M. L. R., Victor, A. L., Hofer, R. R., and Gallimore, A. D. "Effect of Backpressure on Ion Current Density Measurements in Hall Thruster Plumes." *https://doi-org.proxy2.library.illinois.edu/10.2514/1.7713*, Vol. 21, No. 3, 2012, pp. 408–415. doi:10.2514/1.7713.

[3] Nakles, M. R., and Hargus, W. A. "Background Pressure Effects on Internal and Near-Field Ion Velocity Distribution of the BHT-600 Hall Thruster." *44th AIAA/ASME/SAE/ASEE Joint Propulsion Conference and Exhibit*, 2008. doi:10.2514/6.2008-5101.

[4] Frieman, J. D., Walker, J. A., Walker, M. L. R., Khayms, V., and King, D. Q. "Electrical Facility Effects on Hall Thruster Cathode Coupling: Performance and Plume Properties." *Journal of Propulsion and Power*, Vol. 32, No. 1, 2016, pp. 251–264. doi:10.2514/1.B35683/ASSET/IMAGES/LARGE/FIGURE15.JPEG.

[5] Cusson, S. E., Jorns, B. A., and Gallimore, A. D. "Simple Model for Cathode Coupling Voltage Versus Background Pressure in a Hall Thruster." 2017. doi:10.2514/6.2017-4889.

[6] Williams, G. J. . J., Gilland, J. H., Peterson, P. Y., Kamhawi, H., Huang, W., Ahern, D. M., Yim, J., Herman, D. A., Hofer, R. R., Sekerak, M., Gilland, J. H., Peterson, P. Y., Kamhawi, H., Huang, W., Ahern, D. M., Yim, J., Herman, D. A., Hofer, R. R., and Sekerak, M. Wear Testing of the HERMeS Thruster. *Oak Grove Dr*. 3. Volume 301, 4800.

[7] Jambunathan, R., and Levin, D. A. "CHAOS: An Octree-Based PIC-DSMC Code for Modeling of Electron

Kinetic Properties in a Plasma Plume Using MPI-CUDA Parallelization." *Journal of Computational Physics*, Vol. 373, 2018, pp. 571–604. doi:10.1016/j.jcp.2018.07.005.

[8] Nuwal, N., Jambunathan, R., and Levin, D. A. "Kinetic Modeling of Spacecraft Surfaces in a Plume Backflow Region." *IEEE Transactions on Plasma Science*, Vol. 48, No. 12, 2020, pp. 4305–4325. doi:10.1109/TPS.2020.3039110.

[9] Nuwal, N., and Levin, D. A. "Numerical Modeling of Plasma-Surface Interactions in Space Vacuum." 2020. doi:10.2514/6.2020-2153.

[10] Nuwal, N., and Levin, D. A. "Influence of Secondary Electron Emission on Plasma-Surface Interactions in the Low Earth Orbit Environment." *Plasma Sources Science and Technology*, Vol. 30, No. 3, 2021, p. 035015. doi:10.1088/1361-6595/ABE7A1.

[11] Gilland, J. H. (1), Williams, G. J. (1), Burt, J. M. (1), and Yim, J. T. (2). Carbon Back Sputter Modeling for Hall Thruster Testing. 2016.

[12] Polk, J. E., Lobbia, R., Barriault, A., Guerrero, P., Mikellides, I., and Ortega, A. L. "Inner Front Pole Cover Erosion in the 12.5 KW HERMeS Hall Thruster Over a Range of Operating Conditions."

[13] Nakles, M. R., Brieda, L., Reed, G. D., Hargus, W. A., and Spicer, R. L. "Experimental and Numerical Examination of the BHT-200 Hall Thruster Plume." *Collection of Technical Papers - 43rd AIAA/ASME/SAE/ASEE Joint Propulsion Conference*, Vol. 3, 2007, pp. 3041–3058. doi:10.2514/6.2007-5305.

[14] Hillier, A. C., Col, L., Branam, R. D., Huffman, R. E., Szabo, J., and Paintal, S. "High Thrust Density Propellants in Hall Thrusters." 2011. doi:10.2514/6.2011-524.

[15] Choi, M., Yim, J. T., Williams, G. J., Herman, D. A., and Gilland, J. H. "Hybrid-PIC Simulation of Backsputtered Carbon Transport in the Near-Field Plume of a Hall Thruster."

[16] Chinkanjanarot, S. "DENSITY OF AMORPHOUS CARBON BY USING DENSITY DENSITY OF AMORPHOUS CARBON BY USING DENSITY FUNCTIONAL THEORY FUNCTIONAL THEORY." 2014. doi:10.37099/mtu.dc.etds/809.

[17] Williams, J. D., Johnson, M. L., Williams, D. D., Johnson, M. L., and Williams, D. D. Differential Sputtering Behavior of Pyrolytic Graphite and Carbon-Carbon Composite Under Xenon Bombardment.

[18] Yim, J. T. "A Survey of Xenon Ion Sputter Yield Data and Fits Relevant to Electric Propulsion Spacecraft Integration."

[19] Ko, S., Kwon, Y. J., Lee, J. U., and Jeon, Y. P. "Preparation of Synthetic Graphite from Waste PET Plastic." *Journal of Industrial and Engineering Chemistry*, Vol. 83, 2020, pp. 449–458. doi:10.1016/J.JIEC.2019.12.018.

[20] Cai, W., Piner, R. D., Stadermann, F. J., Park, S., Shaibat, M. A., Ishii, Y., Yang, D., Velamakanni, A., An, S. J., Stoller, M., An, J., Chen, D., and Ruoff, R. S. "Synthesis and Solid-State NMR Structural Characterization of ^{13}c-Labeled Graphite Oxide." *Science*, Vol. 321, No. 5897, 2008, pp. 1815–1817.

[21] Cai, W. (1), Piner, R. D. (1), Zhu, Y. (1), Li, X. (1), Ruoff, R. S. (1), Tan, Z. (2), Yang, C. (2), Lu, L. (2), Floresca, H. C. (3), and Kim, M. J. (3). "Synthesis of Isotopically-Labeled Graphite Films by Cold-Wall Chemical Vapor Deposition and Electronic Properties of Graphene Obtained from Such Films." *Nano Research*, Vol. 2, No. 11, 2009, pp. 851–856.

[22] Gibertini, E., Liberale, F., Dossi, C., Binda, G., Mattioli, B., Bettinetti, R., Maspero, A., Fiore, M., Ruffo, R., and Magagnin, L. "Algae-Derived Hard Carbon Anodes for Na-Ion Batteries." *Journal of Applied Electrochemistry*, Vol. 51, No. 12, 2021, pp. 1665–1673. doi:10.1007/S10800-021-01609-2/FIGURES/4.

[23] Ilnicka, A., Skorupska, M., Tyc, M., Kowalska, K., Kamedulski, P., Zielinski, W., and Lukaszewicz, J. P. "Green Algae and Gelatine Derived Nitrogen Rich Carbon as an Outstanding Competitor to Pt Loaded Carbon Catalysts." *Scientific Reports*, Vol. 11, No. 1, 2021. doi:10.1038/S41598-021-86507-5.

[24] Gaefke, C. B., Botelho, E. C., Ferreira, N. G., and Rezende, M. C. "Effect of Furfuryl Alcohol Addition on the Cure of Furfuryl Alcohol Resin Used in the Glassy Carbon Manufacture." *Journal of Applied Polymer Science*, Vol. 106, No. 4, 2007, pp. 2274–2281. doi:10.1002/APP.26938.

[25] Lobbia, R. B., Conversano, R. W., Reilly, S., Hofer, R. R., and Sorensen, R. "Environmental Testing of the HERMeS TDU-2 Hall Thruster." 2018.

[26] Gubernat, M., Tomala, J., Frohs, W., Fraczek-Szczypta, A., and Blazewicz, S. "De-Agglomeration and Homogenisation of Nanoparticles in Coal Tar Pitch-Based Carbon Materials." *Journal of Nanoparticle Research*, Vol. 18, No. 3, 2016, pp. 1–13. doi:10.1007/S11051-016-3362-9.